ELSEVIER

Chemical Engineering Journal 130 (2007) 153–164

Chemical Engineering Journal

www.elsevier.com/locate/cej

Analysis of fluid–elastic-structure interactions in an impinging jet with a dynamic 3D-PTV and non-contact 6D-motion tracking system

T.G. Hwang [a], D.H. Doh [b,*], H.J. Jo [c], M. Tsubokura [d], B. Piao [d], S. Kuroda [d], T. Kobayashi [e], K. Tanaka [f], M. Takei [g]

[a] *Graduate School, Mechanical Engineering, Korea Maritime University, Yeongdo-ku, Busan 606-791, Republic of Korea*
[b] *Division of Mechanical and Information Engineering, Korea Maritime University, Dongsam-dong, Yeongdo-ku, Busan 606-791, Republic of Korea*
[c] *Division of Ocean System Engineering, Korea Maritime University, Dongsam-dong, Yeongdo-ku, Busan 606-791, Republic of Korea*
[d] *Department of Mechanical Engineering and Intelligent Systems, The University of Electro-Communications, Chofu-shi, Tokyo 182-8585, Japan*
[e] *Japan Automobile Research Institute, Tsukuba, Ibaraki 305-0822, Japan*
[f] *Okamoto Co., Bunkyo-ku, Tokyo 113-8710, Japan*
[g] *Department of Mechanical Engineering, Nihon University, Chiyoda-ku, Tokyo 101-8308, Japan*

Abstract

Measurements on pulsed impinging jets with 3D-particle tracking velocimetry (3D-PTV) system and 6-degree-of-freedom (DOF)-motion tracking system were carried out. Pulsed round jets were impinged on an elastic plate and the flow field near the plate was measured with a 3D-PTV system while the motions of the flexible plate was measured with 6D-motion tracking system. The measurement system consists of four cameras, light sources (Nd-Yag laser, Ar-ion laser, Black lamp) and a host computer. The nozzle diameter is $D = 15$ mm and two major experiments have been carried out for the cases of the distances between the nozzle tip to the elastic wall are $z/D = 2.3$ and 6.0. The pulsed jets were controlled by a solenoid valve and were impinged onto an elastic plate (material: silicon, diameter: 350 mm, thickness: 0.5 mm, hardness: 15). The measurement system was synchronized with the valve opening time. The Reynolds numbers were 20,000 and 24,000 when the jets were impinged with the volume velocities. In the first experiments a macroscopic interprets on the flow–structure interactions (FSI) was made using three-dimensional vector fields of the flow and three-dimensional displacements of the elastic plate. In the second experiments a microscopic interprets on the FSI was made using two-dimensional velocity vectors and three-dimensional displacements of the elastic plate. Experimental results showed that the elastic plate moved slightly to the opposite direction of the jet direction at the time of valve opening. It has been shown that the vortices travelling over the surface of the wall made the elastic wall distorted locally.

Keywords: Degree-of-freedom (DOF); Flow–structure interactions (FSI); Three-dimensional particle tracking velocimetry (3D-PTV); Impinging Jet

1. Introduction

A variety of physical phenomena caused by flow–structure interactions (FSI) can be encountered in many engineering problems such as the issues on the stability and responses of aircraft wings, the blood flow properties in the arteries, the responses of bridges and tall buildings onto winds, the vibrations of blades of turbines and compressors, and the oscillations of heat exchangers.

For the theoretical analyses on the FSI problems, two different governing equations are solved together. One is for fluid motions and the other for structure's motions. Furthermore, a kinematic constraint should be imposed along the boundary between the fluid and the structure. Choi [1] proposed the combined formulation, which incorporates both the fluid and structure equations of motion into a single coupled variational equation so that it is not necessary to calculate the fluid force on the surface of structure explicitly when solving the equations of motion of the structure. Therefore, this implicit method is more stable than explicit methods. There are many studies published in the literature using the combined formulation [2–4]. Unfortunately, there is no experimental study for the validations of the previous numerical predictions.

In the meanwhile, impinging jets of various configurations are of great industrial and scientific interests. They are used for many industrial applications usually to enhance heat and mass transfer. They are also found in the process known as gas knife or jet stripping in which impinging plane jets are used to control liquid coatings on the papers or photographic films,

* Corresponding author. Tel.: +82 51 410 4364; fax: +82 51 403 5991.
E-mail address: doh@mail.hhu.ac.kr (D.H. Doh).

1385-8947/$ – see front matter © 2006 Elsevier B.V. All rights reserved.
doi:10.1016/j.cej.2006.06.018

and metallic coatings on continuous galvanizing lines [5]. Impinging jets are also used to extract particles from surfaces either as a cleaning method or to collect samples for chemical analysis, e.g. for detection of explosives or other contraband [6]. Most recently, impinging jets have also gained attention by aerodynamicists dealing with Vertical and Short Take-Off and Landing (VSTOL) aircrafts.

In most studies on impinging jets, the target plate is considered to be rigid as well as fixed so that the vibration of plate, which may be very important in some cases, was neglected. However, in the practical applications there are many cases in which the influences of the motions of the rigid wall or body cannot be neglected. Ellen and Tu found that the uniformity of metal coating on a flexible plate with a jet stripping process depends not only on the pressure but also on the shear stress distributions [5]. However, the vibration of the flexible plate may produce crucial effects on the coating quality due to the FSI problems between the impinging jet and the plate. It is well known that an impinging jet flow becomes turbulent when the jet Reynolds number is bigger than about 300. In nearly all real processes the impinging jet is turbulent because the kinematic viscosity of the working fluids is O(10^{-6} to 10^{-5}) [7]. However, it is not so easy to simulate turbulent impinging jets accurately at high Reynolds number. Simulation itself is a challenging problem at high Reynolds flows. Further, carrying out numerical simulations on the FSI problems is even more difficult at high Reynolds flows no matter how the computer capacity has been better.

The objectives of this paper is to carry out an experimental analyses qualitatively and quantitatively on the FSI between an impinging jet and a flexible target plate by constructing a measurement system that can measure simultaneously the plate's motions and the flow fields contacting the plate.

2. Measurement system and principles

2.1. Measurement system

The overall measurement system for the analyses of flow–elastic-structure interactions of a jet is shown in Fig. 1. The jet is impinged onto a thin elastic plate. Fig. 2 is the used elastic plate (material: silicon, diameter $D = 400$ mm, thickness: 0.5 mm, hardness: 15). The diameter of the jet nozzle is $D = 15$ mm. Measurements were carried out to obtain the motions of the elastic plate onto which a pulsed jet was impinged and to get the vector fields of the jet flow.

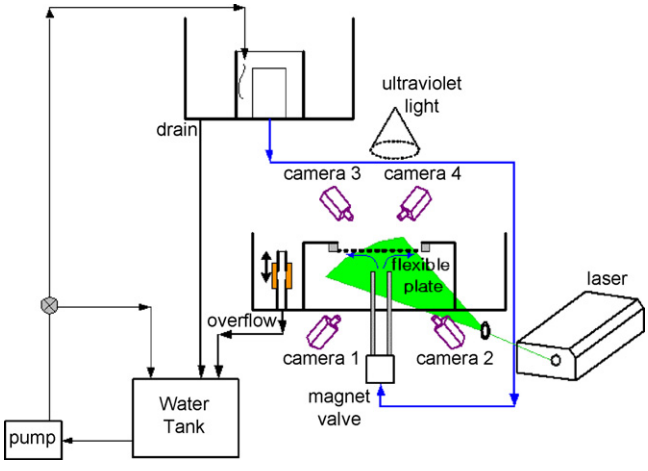

Fig. 1. Schematic of the overall measurement system.

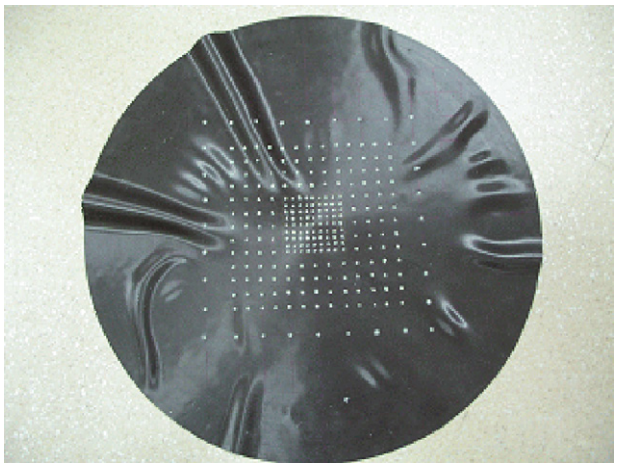

Fig. 2. Used flexible plate ($D = 400$ mm, $t = 0.5$ mm).

Measurement of three-dimensional vector field of the jet flow is attained by tracking three-dimensional positions of the particles (nylon, specific gravity: 1.02, diameter: 100–150 μm). Measurement of 6DOF-motions of the elastic plate is attained by tracking three-dimensional positions of the tracking objects marked with phosphorescent paint (diameter: 2 mm) on the surface on the plate as seen in Fig. 2. The measurement principles for both systems are explained in the next section.

Two measurement systems have been constructed for two kinds of experiments for macroscopic and microscopic analyses on FSI. For macroscopic analyses, four cameras have been arranged as seen in Fig. 1 for simultaneous measurements for 3D flow fields and 6DOF-motion fields. Two cameras (Kodak ES 1.0, 1008 × 1018 pixels, 30 fps), cameras 1 and 2, capture images of the jet flow fields and the other two cameras (Photorn, Fastcam-X 128 PCI, 1024 × 1024 pixels, 125 fps), cameras 3 and 4, capture the images of the plate's motion.

The distance between the nozzle and the elastic plate in case of macroscopic analyses is $z/D = 2.3$ (z is the vertical coordinate of the jet blowing direction). For microscopic analyses, three cameras with high-speed frame rate and high-resolution have been used. One camera (Photron APX-RS, 1024 × 1024 pixels, 1500 fps), camera 1, captures images of the jet flow fields and other two cameras (Photorn, Fastcam-X 128 PCI, 1024 × 1024 pixels, 250 fps), cameras 3 and 4, capture the images of the plate's motion. The distance between the nozzle and the elastic plate in case of macroscopic analyses is $z/D = 6.0$. Two-dimensional flow fields are obtained by using the image of camera 1 and 6DOF-motion fields are obtained by using the image of cameras 3 and 4.

Time consecutive four (or three images) captured by the four (or three) cameras for each analysis are transferred to a host computer (Pentium IV, 3 GHz) to calculate the centroids of the images of the tracking objects (the marks on the elastic plate and the particles in the flow field). The photographic

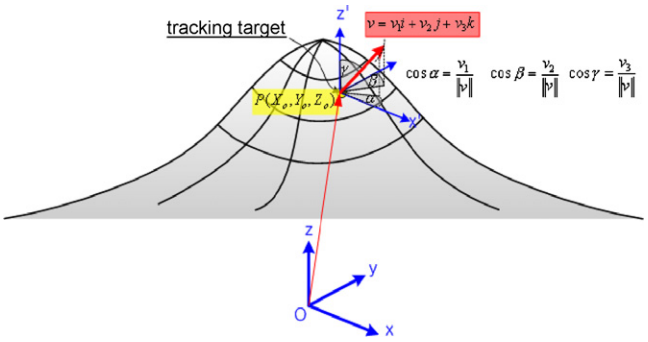

Fig. 3. The schematics of the 6-degree-of-freedom (DOF)-motions.

coordinates of the objects' centroids are used for the calculation of three-dimensional vector fields and 6DOF-motion fields. The definition of the 6DOF-motion fields is shown in Fig. 3 for the case of the elastic plate's motions, and Fig. 4 explains the general 6DOF motions in which three translational motions and three rotational motions are composed of. Detailed process for the calculation of three-dimensional motional properties of the objects (particles and targets) is explained in the next section.

2.2. Principle of simultaneous measurements on 3D-flow field and 6DOF-motion field

Fig. 5 shows the principle of flow–structure interactions measurements. The measurement system mainly consists of two parts, one for three-dimensional vector fields of the flow and the other for 6-degree-of-freedom motions of the structure contacting the flow. Each system has two cameras and all four cameras are synchronized for simultaneous image capturing. Since all

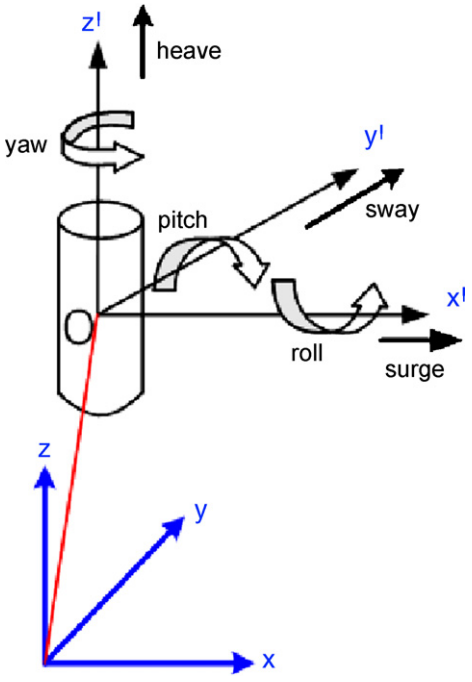

Fig. 4. Explanations of 6DOF.

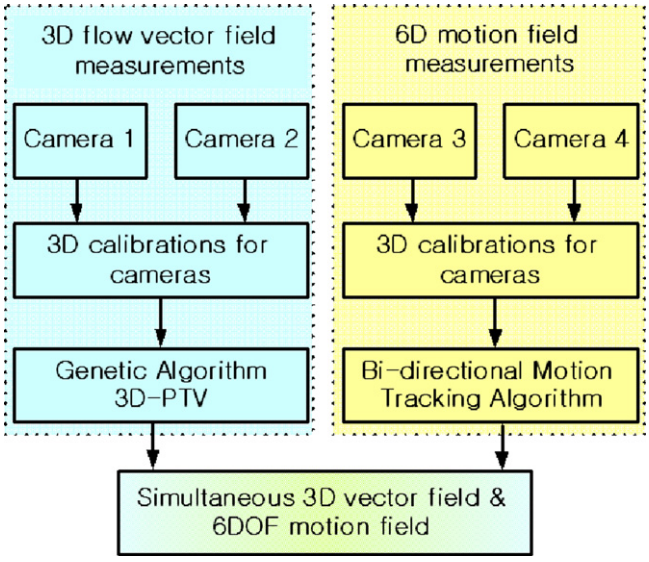

Fig. 5. Principle of flow–structure interactions (FSI) measurements.

cameras' coordinates are different from that of the absolute coordinate (physical coordinate), it is necessary for the cameras to be calibrated onto the absolute coordinate in order to measure objects' three-dimensional positions on the absolute coordinate with two cameras. This process is called camera calibration. In this study, the 10-parameter method [8] has been adopted for the camera calibration. For the measurement of three-dimensional vector field two cameras' images (cameras 1 and 2) were used and the genetic algorithm (GA) based 3D-PTV [8] algorithm has been adopted for the analysis on these images. For the measurement of 6-degree-of-freedom (DOF)-motion field two cameras' images (cameras 3 and 4) were used and the 'bidirectional searching algorithm' [9] has been used for the analysis on these images. Fig. 3 shows the general definition of the 6DOF-motion, and Fig. 4 shows how 6DOF is obtained. Firstly, the three-dimensional position of the target P(X_0, Y_0, Z_0) and the vector (v) are obtained from the 3D-particle tracking velocimetry (PTV) calculations [8]. Secondly, the directional angles are obtained.

2.2.1. Camera calibrations and calculations of 3D positions of objects

In order to obtain the three-dimensional positional information of the seeding particles of the flow field and the targets marked on the elastic plate, their image centroids were used as photographic coordinates. These photographic coordinates and their absolute coordinates were used to calculate the parameters of the cameras. For camera calibration two kinds of calibrators, volume type and plate type, have been used.

The volume type has 42 landmarks as shown in Fig. 6. It was used for the calibration of cameras 1 and 2 for 3D flow field measurements. These landmarks are sphere balls (diameter: 1.0 mm, painted with white colour) have been arranged three-dimensionally on a table (80 mm × 110 mm × 10 mm; $W \times L \times T$) with steel bars (diameter: 0.8 mm, its lengths are various). The three-dimensional positions had already been

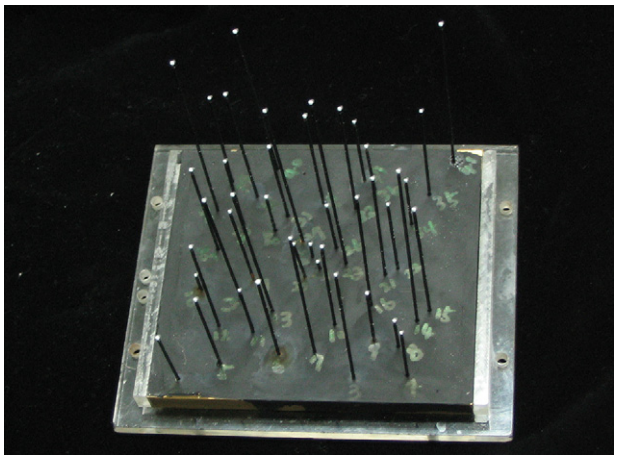

Fig. 6. Volume type calibrator.

measured by an optical measurement system (EG 2020CNC, precision = 1/1000 mm) in which a high-definition camera (2048 × 2048 pixels) is installed onto the end of a high-precision traverse, and the images of the targets are magnified four times bigger than the originals to calculate exact centers of the targets. The plate type was used for the calibration of cameras 3 and 4 for the measurement of 6DOF-motion field of the elastic plate. It has 289 grids on a flat plate (200 mm × 200 mm × 10 mm; $W \times L \times T$) with 10 mm interval. This calibrator is traversed to construct three-dimensional landmarks in space. Fig. 7 shows a picture of the calibration work with the plate type.

In this study, 10 parameters (6 exterior parameters: dis, α, β, γ, m_x, m_y, and 4 interior parameters: c_x, c_y, k_1, k_2) were obtained. The Greek symbols (α, β, γ) represent the tilting angles of the axes of the photographic coordinates against the absolute axes. Fig. 8 shows a coordinate relation when the photographical axes had been set to parallel with the absolute coordinate by tilting with the angles (α, β, γ). (X, Y, Z) represents the absolute coordinate, and (x, y, z) represents the photographical coordinate of the image centroids of the targets and the seeded particles. The notation 'dis' means the distance between the origin O(0, 0, 0) and the principal point (X_0, Y_0, Z_0) of the camera.

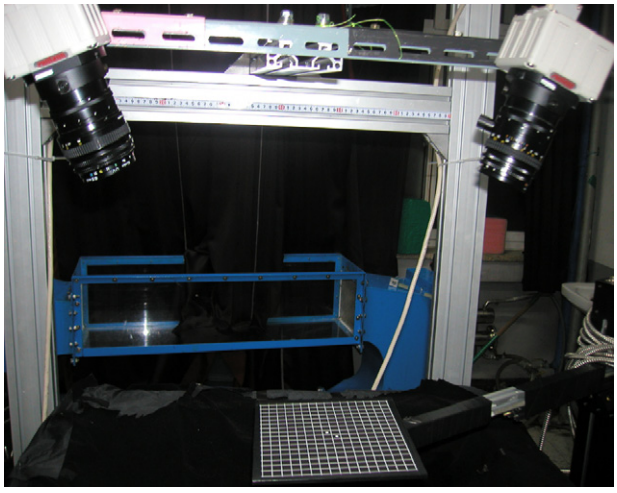

Fig. 7. Plate type calibrator.

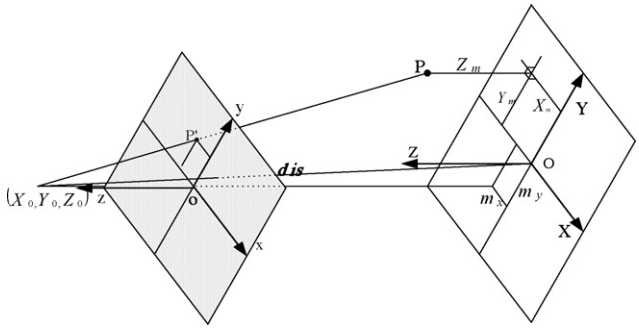

Fig. 8. Relations of camera parameters on the absolute coordinate and the photographical coordinate.

The coordinate (X_m, Y_m, Z_m) represents the position of the point P when the camera coordinate is rotated with the tilting angles to make the collinear equation on one line as shown in Fig. 4. The m_x, m_y mean the point at which the normal vector from the origin O(X_0, Y_0, Z_0) of the camera coordinate meets with the X–Y plane. The collinear equation for every point between the two coordinates is expressed as Eq. (1). c_x and c_y are the focal distances for x and y components of the coordinate. Δx and Δy are the lens distortions as expressed as Eq. (2). Eq. (1) can be converted to the following Eq. (3). Since this equation is a strong non-linear, an improved Gauss–Newton calculation method [4] was adopted to obtain all necessary parameters using the above two equations in Eq. (3).

$$x = c_x \frac{Y_m - m_x}{\sqrt{\mathrm{dis}^2 - m_x^2 - m_y^2} - Z_m} + \Delta x,$$

$$y = c_y \frac{Y_m - m_y}{\sqrt{\mathrm{dis}^2 - m_x^2 - m_y^2} - Z_m} + \Delta y \tag{1}$$

$$\Delta x = \left(\frac{x}{r}\right) \times (k_1 r^2 + k_2 r^4), \qquad \Delta y = \left(\frac{x}{r}\right) \times (k_1 r^2 + k_2 r^4),$$

$$r = \sqrt{x^2 + y^2} \tag{2}$$

$$F = c_x \frac{X - m_x}{\sqrt{\mathrm{dis}^2 - m_x^2 - m_y^2} - Z_m} - (x - \Delta x) = 0,$$

$$G = c_y \frac{X - m_x}{\sqrt{\mathrm{dis}^2 - m_x^2 - m_y^2} - Z_m} - (y - \Delta y) = 0 \tag{3}$$

Once all camera parameters are obtained, the relations between the photographic coordinate and the absolute coordinate of the targets' image or the particles' image can be expressed as the following Eq. (4):

$$\begin{bmatrix} X \\ Y \\ Z \end{bmatrix} = \mathrm{M}_\mathrm{M}^{-1} \begin{bmatrix} X_m \\ Y_m \\ Z_m \end{bmatrix} = \mathrm{B} \begin{bmatrix} X_m \\ Y_m \\ Z_m \end{bmatrix} \tag{4}$$

Here, $\mathrm{M_M}$ is the matrix for the rotational transformation and B is its inverse matrix. (X_m, Y_m, Z_m) is expressed in the form of

Eq. (5).

$$X_m = \frac{x - \Delta x}{c_x} t + m_x, \qquad Y_m = \frac{y - \Delta y}{c_y} t + m_y,$$

$$Z_m = d - t, \qquad d = \sqrt{\mathrm{dis}^2 - m_x^2 - m_y^2} \tag{5}$$

If the center of the camera is set to a vector (X_0, Y_0, Z_0), the collinear equation for one target (or particle) can be simplified as $X_P(X, Y, Z) = (a_1 t + X_0, a_2 t + Y_0, a_3 t + Z_0)$. The cross-sectional points constructed from the following two collinear equations for the two cameras can be defined as the three-dimensional positions in the absolute coordinate.

$$X_A = (a_{11}k + b_{11}, a_{12}k + b_{12}, a_{13}k + b_{13})$$
$$X_B = (a_{21}s + b_{21}, a_{22}s + b_{22}, a_{23}s + b_{23}) \tag{6}$$

Here, t and s are obtained by the least square method (LSM). Since the cross-sectional points do not always intersect on one point, the below Eq. (7) was used for the definition of the last three-dimensional position of the targets (or the particles), which implies the midpoint of the shortest distance between the two collinear equations expressed as Eq. (6).

$$\begin{bmatrix} X_P \\ Y_P \\ Z_P \end{bmatrix} = \frac{1}{2} \left\{ \begin{bmatrix} X_A \\ Y_A \\ Z_A \end{bmatrix} + \begin{bmatrix} X_B \\ Y_B \\ Z_B \end{bmatrix} \right\} \tag{7}$$

Here, X_A, Y_A and Z_A represent the absolute coordinates for camera A defined by Eq. (6). X_B, Y_B and Z_B are for camera B.

2.2.2. 3D-flow field measurements

Once the parameters of the cameras 1 and 2 as shown in Fig. 1 are obtained by the camera calibrations, any seeding particle's three-dimensional position can be calculated with the photographical coordinates of its images and the camera parameters. Three-dimensional vector is obtained by dividing the three-dimensional displacements of the particles in the flow by a time interval, $\vec{v} = \vec{S}/\Delta t$. The time interval is known from the camera's frame rate. The displacement vector $\vec{S}$ is obtained from the distance of particle's moving during the period of two consecutive image frames. To calculate three-dimensional displacement, the particles' positions at the first image and at the second image should be obtained.

The principle of obtaining the three-dimensional positions of particles is shown in Fig. 9. Point 'P' is the intersected position of the two collinear vectors (→ O1p1 and→ O2p2). 'p1' and 'p2' are the images of particle 'P'. The photographical coordinates of p1 and p2 are obtained by calculating the centre of the area of the particle's image. The displacements of the particle 'P' (blue coloured) during the period of two image frames are the distances between the position 'P' and the other one among the red points. Since there are many candidates of particles that are thought as the same particle between the first and the second images as seen in Fig. 9, searching process for the same particle pair between two consecutive image frames is necessary. The genetic algorithm based 3D-PTV algorithm [8] has been used for this. This algorithm carries out an optimization process of finding particles' pairs with two fitness functions. One is the continuity equation of fluid flows and the other is the distance between the collinear vectors. Judgements for the correctness of particle pairing are made when these two fitness functions have minimum values. Four major GA operators, isolation, reproduction, crossover and migration have been introduced in this study. Two sets of photographical coordinates of the vector start points and the vector terminal points were regarded as the chromosome in the genetic algorithm. The initial population was generated through a calculation process in which a threshold value was introduced to discriminate the worst particle pairs that had bigger values than a threshold. After the initial population was generated, an isolation process was operated using a threshold distance. The particle pairs having a value larger than the threshold were isolated to the unselected group. Next, a reproduction process was made. In the reproduction process, a fitness function based on the continuity concept was used for a refinement of the selected group. Finishing the reproduction process, a crossover process was adopted. In this process, the photographical data of the two-dimensional vectors of each camera were exchanged and an elimination process was made referencing the threshold value again. In order to give a survival chance to the particles sorted into the inferior group up to now, a migration process was adopted. This process is similar to the initialization process. The above processes were repeated up to 10–15 generations. The threshold value here was set to 0.5 mm and the crossover portion was set at 15% among the whole chromosomes generated. During the calculation of GA, operators such as, isolation, reproduction, crossover and migration (this concept belongs to mutation) were recursively used until the last optimized solution of the fitness functions were obtained, which implies the pairs of particles were decided. The three-dimensional velocity vectors were then obtained by dividing the distances between the last paired particles by the time interval Δt as mentioned in the above. More detailed calculation procedure for the GA based 3D-PTV is well explained in the reference of Doh et al. [8].

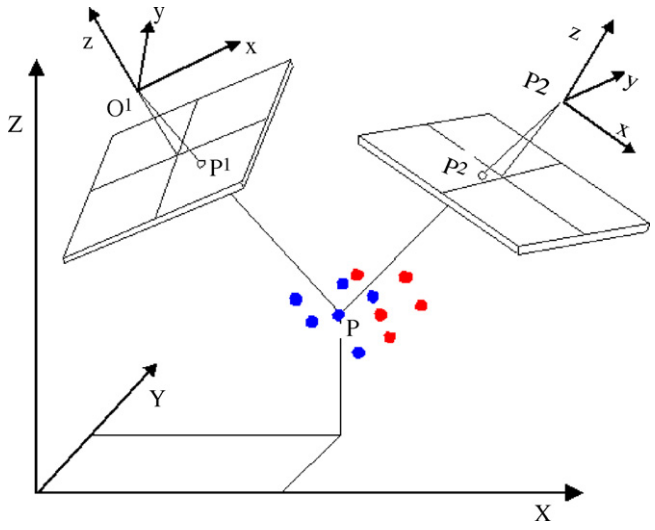

Fig. 9. Principle of particles' identification with two camera system.

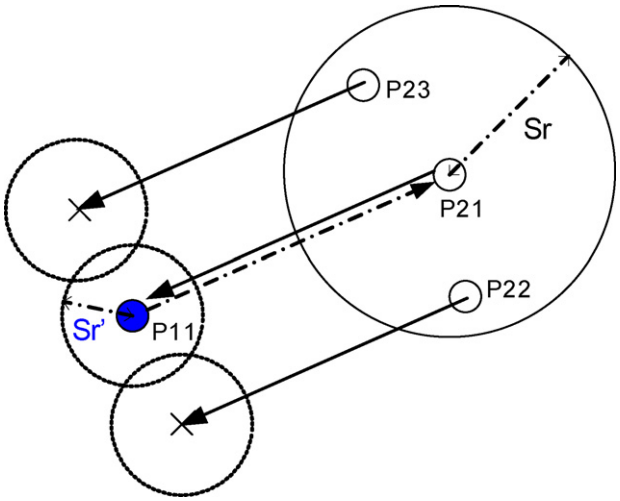

Fig. 10. Principle of bidirectional searching algorithm.

2.2.3. 6DOF-motion field measurements

Once the parameters of the cameras 3 and 4 as shown in Fig. 1 are obtained by the camera calibrations, three-dimensional positions of the targets marked with phosphorescent paint on the surface of the elastic plate can be calculated with the photographical coordinates of their images and the camera parameters. For the calculation of 6DOF-motion the same targets on the elastic surface should be tracked with temporal change. In this study, a "bidirectional searching algorithm" as shown in Fig. 10 has been used. In this algorithm, it is regarded that the same object between the two consecutive image frames has been found on the condition that the original object's image (P_{11}) is seen in a certain area (Sr′) of which center point is defined by the end point of the vector from the object P_{21} (dotted line from P_{21}) in the search area (Sr). In this study, Sr was set to 20 pixels and Sr′ to 15 pixels.

3. Experiments on pulsed impinging jets and FSI analyses

Two cases of experiments were carried out. As the first case, the distance between the jet nozzle and the elastic plate was set to $z/D = 2.3$ ($D = 15$ mm), and the solenoid valve installed at the inlet of the jet nozzle was opened once and was closed after 1.0 s (single-pulsed jet flow). The Reynolds number in this case was about 20,000 with the mean flow velocity. In the second case, the distance was set to $z/D = 6.0$. The valve opening time was also set to 1.0 s. The Reynolds number was about 24,000 with the mean flow velocity.

The first case corresponds to macroscopic experiments and the second corresponds to microscopic experiments. In macroscopic experiments, three-dimensional vector fields and 6DOF-motion fields are obtained for the first case, the single-pulsed jet. Since the number of instantaneous three-dimensional vectors is not so high enough to resolve the interactions quantitatively between the small-scaled vortices and the elastic impinging plate, qualitative evaluations on the FSI phenomena in the jet has been made. In microscopic experiments, two-dimensional vector fields on the centre plane of the jet were obtained by the use of 2D-PIV [10] and 6DOF-motion fields of the elastic plate were also obtained simultaneously.

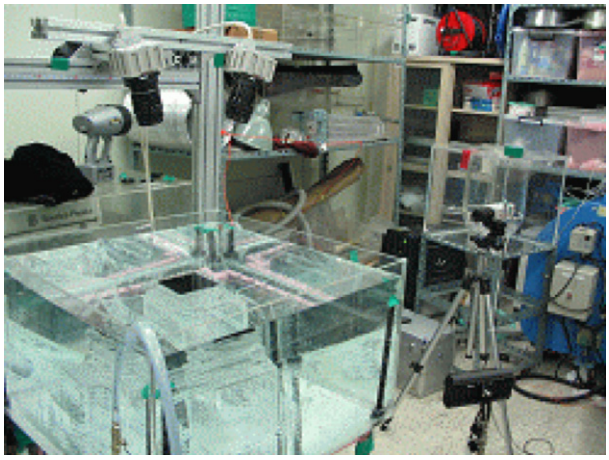

Fig. 11. Macroscopic experimental setup (four camera system).

3.1. Macroscopic experiments on a single-pulsed impinging jet and FSI analyses

Macroscopic experiments were carried out as follows. As explained in the above, camera calibration process was taken at first in the same manner of Section 2.2.1. Two kinds of camera calibrators as shown in Figs. 6 and 7 were used. The coordinate origins of the two calibrators were transformed to the location of the tip centre of the jet nozzle. After camera calibration tracer particles were seeded into the water vessel as shown in Fig. 11 with amount of 0.05% water volume fraction. Completing seeding the particles ($Ø = 100$–150 μm, specific gravity = 1.02) into the water tank (acryl, 700 mm × 700 mm × 700 mm; $W \times L \times H$), the impinging plate (silicon, diameter: 400 mm, thickness: 0.5 mm, hardness: 15) as shown in Fig. 12 is assembled onto its frame holder of the water tank. For visualizations of the flow field Nd-Yag laser (120 mJ, 15 Hz) was used. For visualization of the motions

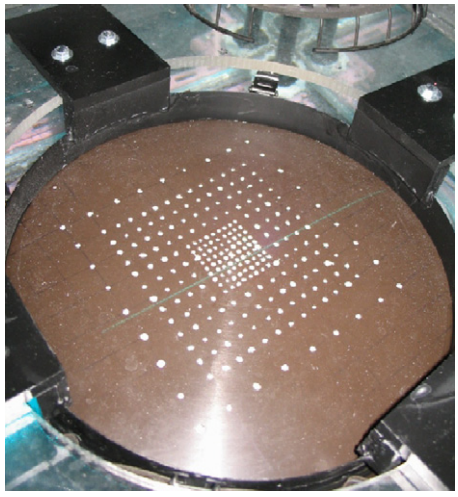

Fig. 12. Assembled elastic plate.

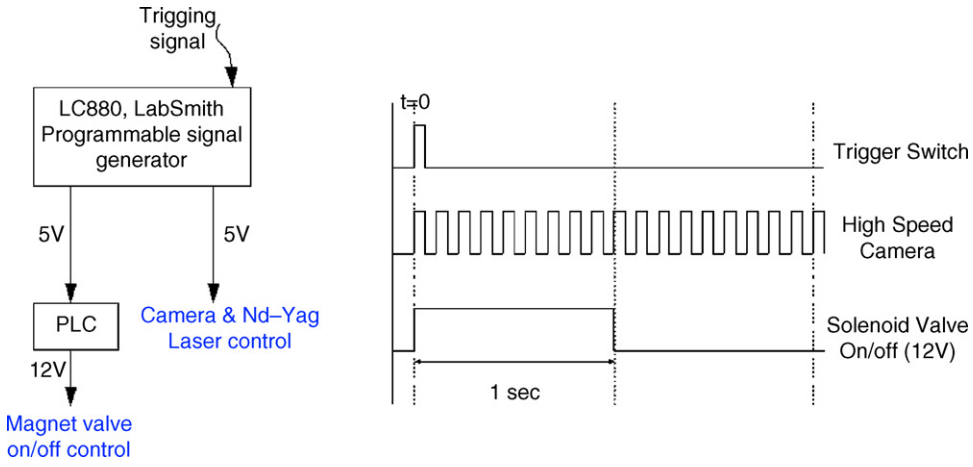

Fig. 13. Control system and activation signals for valve opening and measurement system.

of the elastic plate a black lamp (200 W, ultraviolet light) was used to energize phosphorescent targets painted on the surface of the elastic plate in order to enhance their visibility. After assembling the impinging plate main experiments in which activating the jet and taking the images of the four cameras into the hard memory of the host computer were carried out.

Since some particles' density is not just the same as that of water, particles suspended in neutral positions are not so many, which is not desirable for resolving the spatial flow structure, additional particle seeding was made at the head tank inlet during the main experiments. The hydraulic head was used to produce a jet flow. The pulsed jet was controlled by opening the solenoid valve electronically.

The schematic of the control system and the relation of the timing signals of the measurement system are shown in Fig. 13. When a trigging signal put into the system controller (LC880)

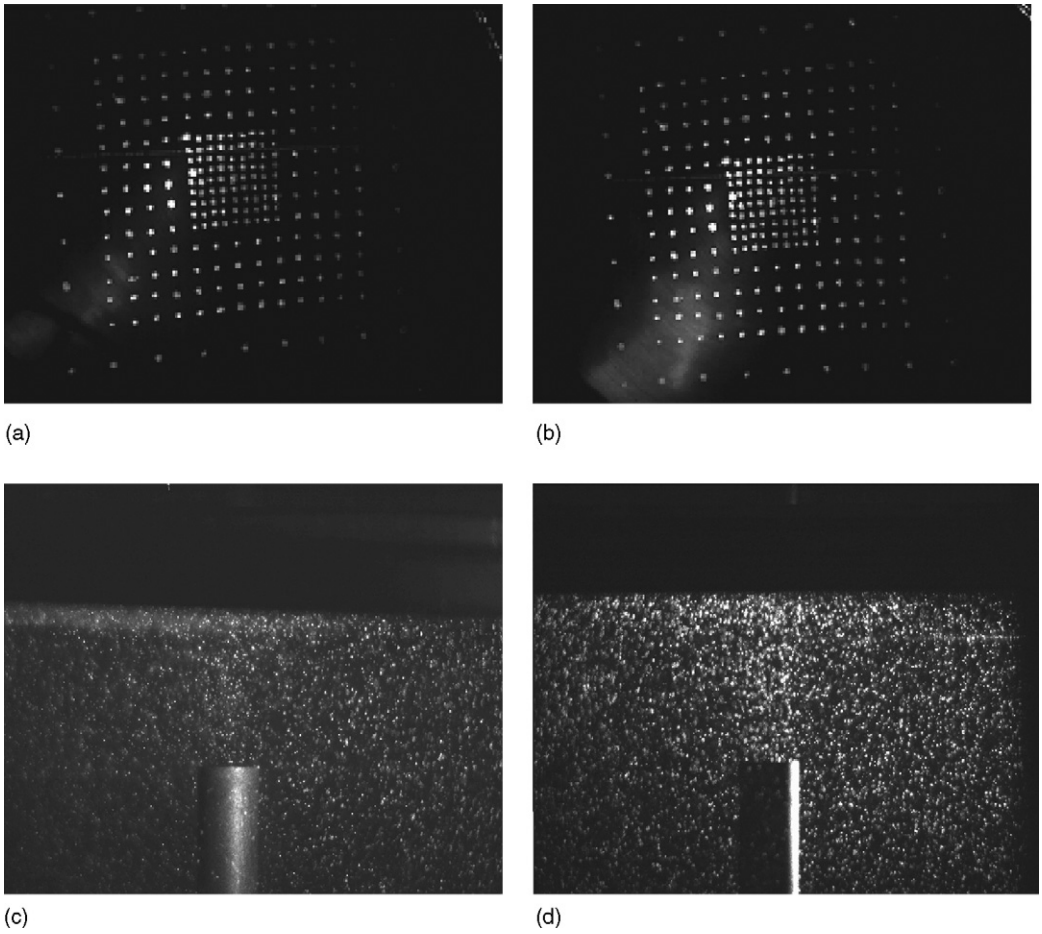

Fig. 14. Instantaneous images captured by the: (a) camera 3, (b) camera 4, (c) camera 1 and (d) camera 2.

in which signal delays can be made freely, two control signals (5 V) are generated from this controller, one is for activation of the programmable logic controller (PLC) and the other is for activation of the camera and laser system. The opening time of the solenoid valve at the inlet of the jet pipe (inner diameter: 15 mm) can be controlled by this PLC signal. Accordingly, all systems are operated in synchronous. The valve on/off time duration in macroscopic experiments is 1.0 s.

Instantaneous experimental images captured by the four cameras are shown in Fig. 14. The upper two images, (a) and (b), were taken by the cameras 3 and 4, and the two below images, (c) and (d), were taken by the cameras 1 and 2. Three-dimensional vector fields and 6DOF-motion fields were obtained by using the centroids of objects' images (marked targets, particle) of the cameras 1–4.

Fig. 15 shows the results obtained by the 6DOF-motion tracking system for the case of $z/D = 2.3$. The results are the displacements [mm] of vertical direction (z-axis) at the centre of the elastic plate versus time proceeding. x-Axis of this graph is the camera's frame time. Since the capture interval of the camera used for 6DOF-motion measurements was 1/125 s, the time at the image frame 500 implies $500 \times (1/125) = 4$ s after starting recording of camera images. There is a slight downward motion of the elastic plate at the time of t_1 (FN, frame number: 406) even if the jet has just started blowing upward toward the plate. It is

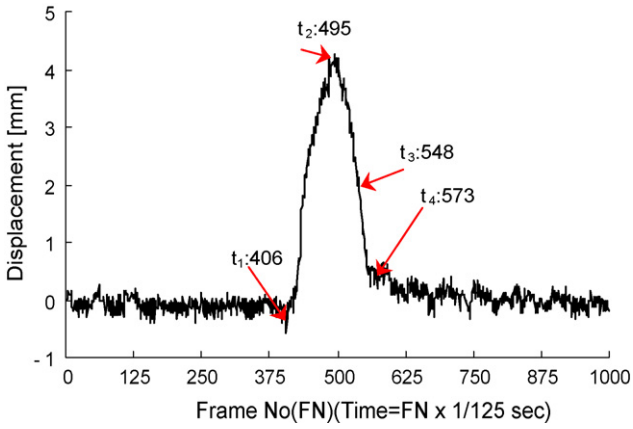

Fig. 15. Displacements of the center point of the elastic plate to normal direction ($z/D = 2.3$).

construed from this phenomenon that the fluid from the jet nozzle produced an entrainment of the surrounding fluids, which makes an increase of mass flow rate and this increased mass sweeps outward along the elastic wall, eventually producing a 'pressure drop' near the stagnation point.

Fig. 16 shows measured three-dimensional vector fields of the jet flow obtained by the GA-3D-PTV at four different instances as indicated in Fig. 15 as t_1 (FN: 406), t_2 (FN: 495), t_3 (FN: 548)

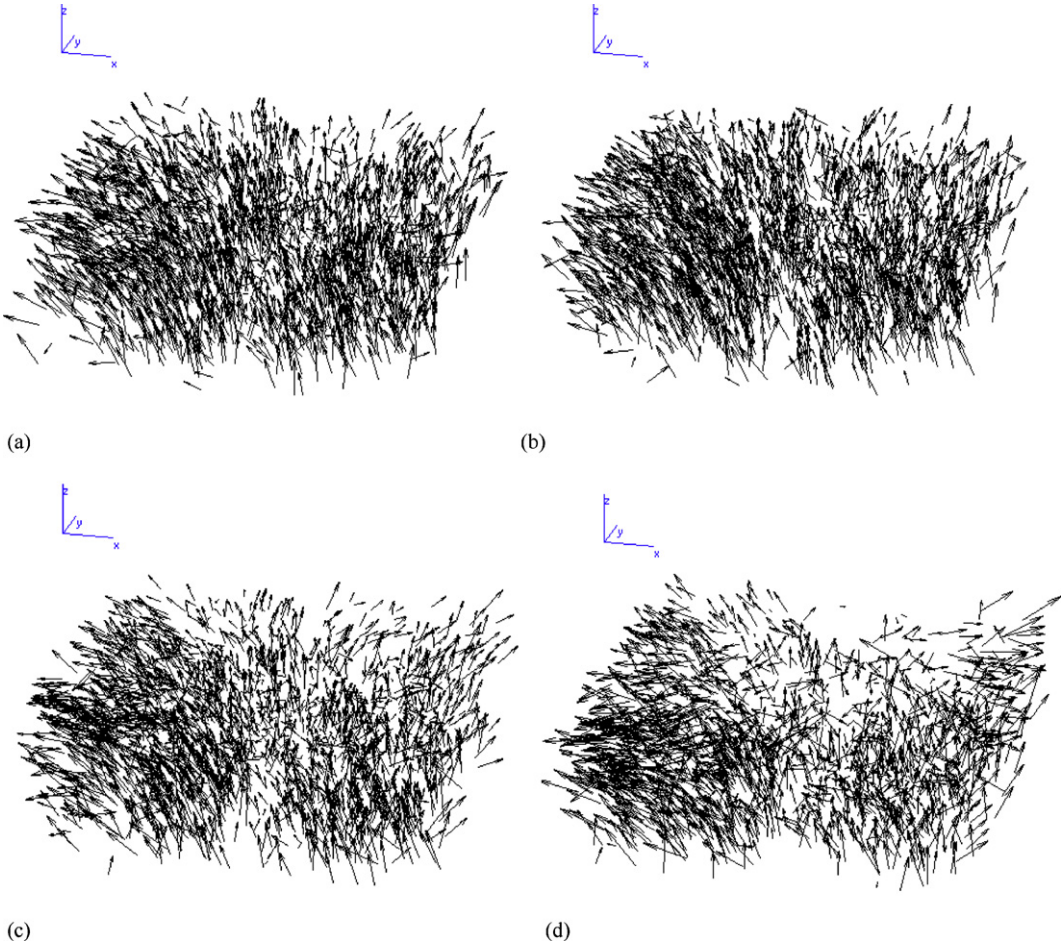

Fig. 16. Instantaneous three-dimensional vector distributions at the times in Fig. 15: (a) at time = t_1, (b) at time = t_2, (c) at time = t_3 and (d) at time = t_4.

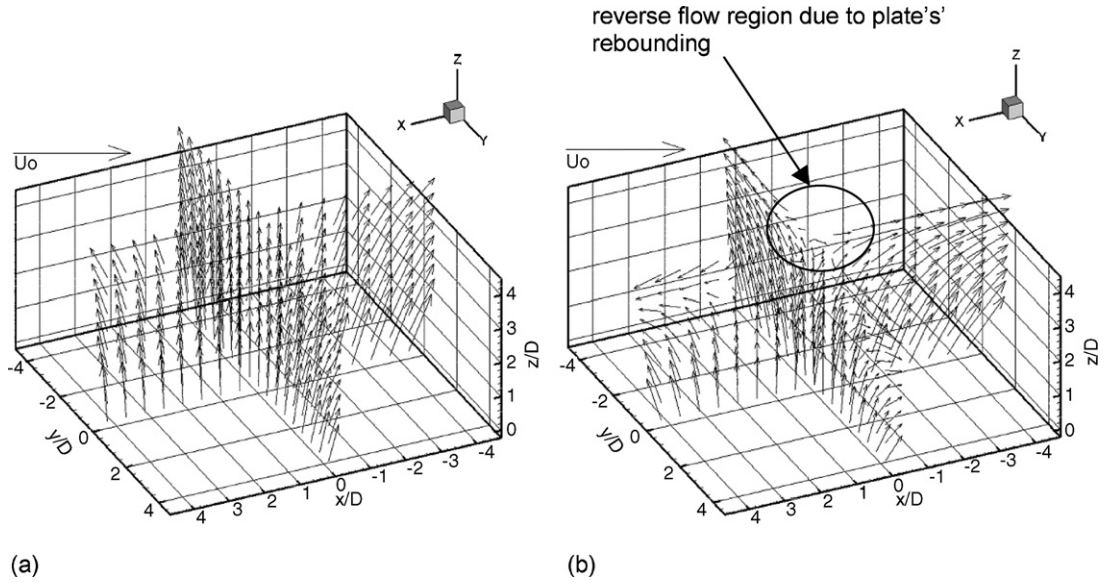

Fig. 17. Three-dimensional vector distributions on grid (17 × 17 × 9): (a) t_2—at maximum displacement; (b) t_4—at rebounded state.

and t_4 (FN: 573). About 2000–2500 instantaneous 3D velocity vectors were obtained. The time difference between t_1 and t_4 is about 1.34 s, which means that there is a 0.34 s difference from the valve opening time 1.0 s. It seems that the acceleration effects of the pulsed jet extend the duration by producing entrainments of the surrounded fluids. In order to investigate the FSI characteristics qualitatively, the instantaneous 3D vectors were interpolated onto 17 × 17 × 9 grids.

Fig. 17 shows the interpolated 3D vector distributions on the centre planes at the time of t_3 (at which the plate has reached the maximum displacement) and t_4 (at which the plate has rebounded to the original flat state). All vectors were non-dimensionalized with U_0, the mean velocity of jet exit. As seen in Fig. 17a, the flow near the stagnation region goes upward at the maximum displacement of the plate. At t_4 when the plate comes to the original flat state, the flow near the stagnation region goes downward. It is thought that the reverse flow near the stagnation region is due to the fact that rebounding of the elastic plate pushed the flow downward. This can be regarded as one of the most conspicuous FSI phenomenon. It could be said that the results obtained in macroscopic experiments showed qualitatively reasonable ones. Quantitative investigation into the FSI near the elastic wall is made in the microscopic experiments.

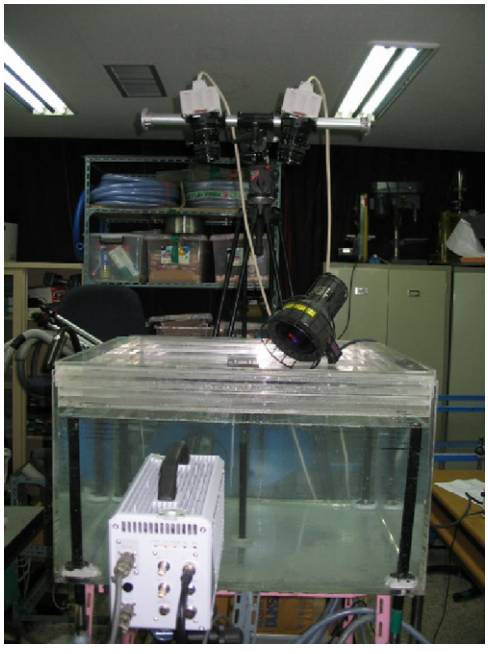

Fig. 18. 6DOF-motion and 2D-PIV system.

3.2. Microscopic experiments on single-pulsed impinging jet and FSI analyses

In order to investigate more detailed flow–structure interaction phenomena near the elastic plate, analysis of higher temporal and spatial resolution for the obtained velocity vector is needed, which implies a microscopic experiment is necessary.

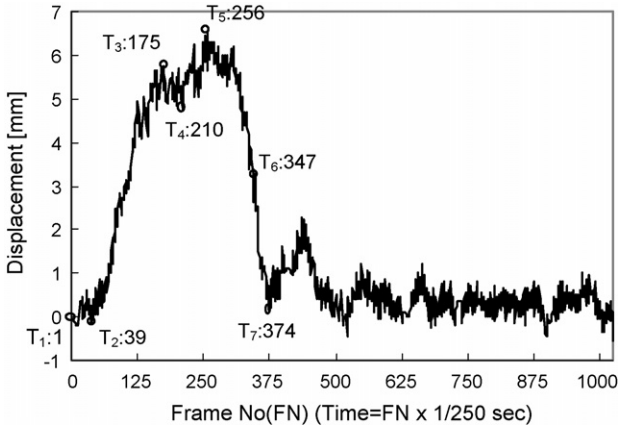

Fig. 19. Displacements of the center point of the elastic plate to normal direction (z/D = 6.0).

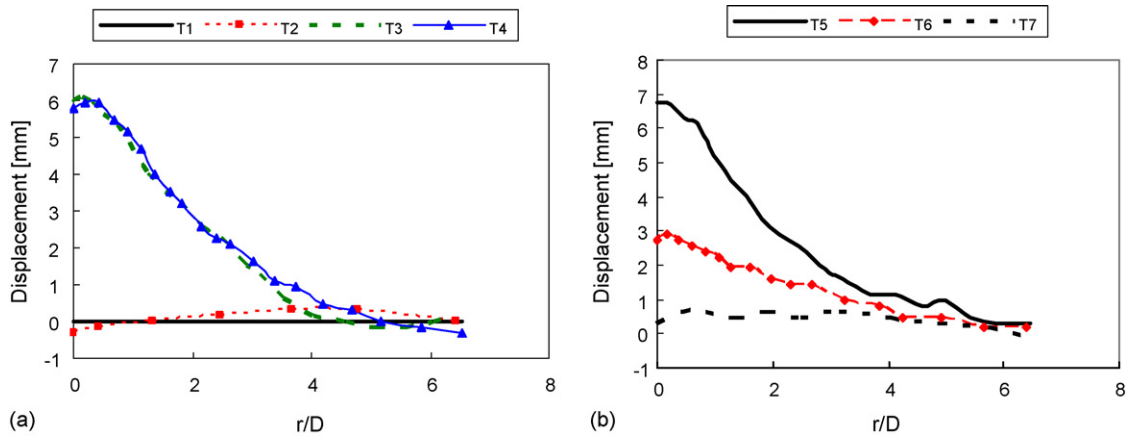

Fig. 20. (a and b) Temporal changes of the plate's profiles at T_1–T_7.

To do this, the frame rates of the cameras used for imaging the motion fields and the jet flow fields were increased to 250 fps and 1500 fps from 125 fps and 30 fps, respectively. Further, since 2D-PIV analysis generally provides higher spatial vector maps than 3D-PTV does, though the results of 2D-PIV are on two-dimensional plane rather than on three-dimensional volume, 2D-PIV measurements were replaced with 3D-PTV measurements for microscopic analysis on the FSI. Fig. 18 shows the picture of 6DOF-motion and 2D-PIV measurement system.

Microscopic experiments were carried out as follows. The camera calibration works have been carried out at first as in the same manner made in the macroscopic experiments. Other experimental procedure and apparatus are the same as those in macroscopic experiments except the followings. The distance was newly set to $z/D = 6.0$ from 2.3. As a light source for flow visualization Ar-ion laser (5 W, continuous) was used. The on/off time of the solenoid valve on/off is in Fig. 13. The valve opening duration is 1.0 s.

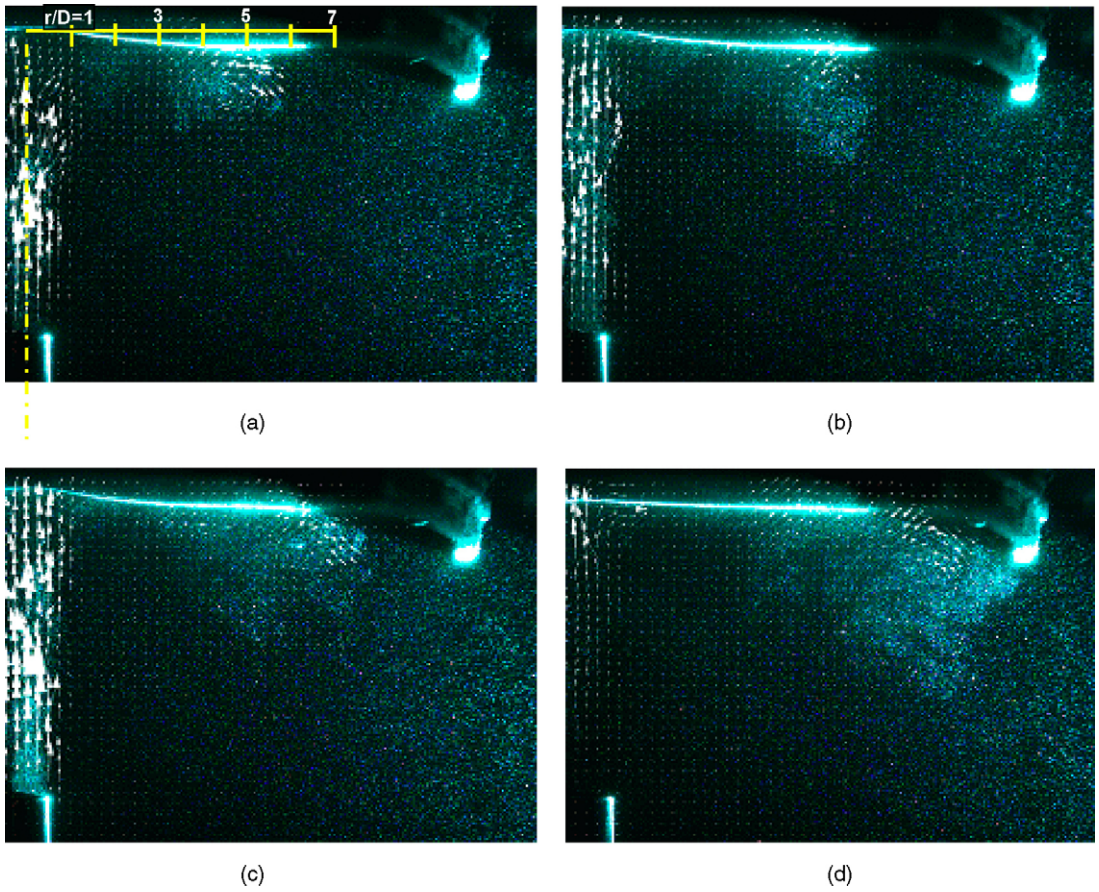

Fig. 21. Distributions of velocity vectors at the instances of: (a) $t = T_3$, (b) $t = T_4$, (c) $t = T_5$ and (d) $t = T_6$ as indicated in Fig. 19.

The temporal evolutions of the displacements of the center point of the elastic plate to normal direction is shown in Fig. 19. The instances from T_1 to T_7 correspond to frame number (FN) 1, 39, 175, 210, 256, 347 and 374. Since the camera's frame rate is 1/250 s, the frame number 374 corresponds to about 1.49 s (374 × (1/250)) after valve closing. The difference of the valve opening time 1.0 s and 1.49 s seems to be from the acceleration effects of the pulsed jet as mentioned in the case of $z/D = 2.3$.

T_1 is the time of valve opening. At the time T_2, just after valve opening, there is a slight downward motion. This phenomenon was also seen in the case of $z/D = 2.3$. By the way, the duration (T_2–T_7) showing high frequency is longer than that in the case of $z/D = 2.3$ (see Fig. 15). The long period of high frequencies implies that the jet flow having high frequencies has impacted on the elastic wall. It is related to the fact that the jet flow develops to more complex and high-frequency flow when the distance between the jet nozzle and the wall is long. It was also seen from the experiments that the vortices descended from the jet nozzle become very unstable near the stagnation region, and which makes the elastic plate fluctuate up and down irregularly, eventually making the motion of the plate fluctuate with high frequency between T_2 and T_7.

The temporal changes of the profiles of the elastic plate's motion at the instances of T_1–T_7 along the center line of the plate are shown in Fig. 20. At T_1 the shape of the plate is flat. As indicated in previous, the displacement of the centre point of the plate goes downward slightly at T_2 even if the jet has been started blowing out toward upward. That is, the displacement at r/D at T_2 is negative value. It also seems that a 'slight pressure drop' near the stagnation point occurs at T_2 as in the case of $z/D = 2.3$. At the region of $r/D > 4.0$, the displacements of the plate seem to be relatively smaller than in the region of $r/D < 4.0$.

Fig. 21a–d shows the velocity vector distributions at the instances T_3–T_6 as indicated in Fig. 17. At T_3–T_5 the profiles of the elastic plate become a 'bell shape'. Interesting thing is that a big primary vortex generates near $r/D = 4.0$ at which the bell shape ends (bell edge). At T_6 it can be seen that the vortex that has descended from $r/D = 4.0$ swept away outward due to the downward pushing force of the elastic plate.

The flow–structure interactions of the elastic plate due to the vortices that had been descended from the impinged jet is shown in Fig. 22a–c. These figures have been presented to show a detailed influence of the vortices to the elastic wall. The vortex that had been generated at the bell edge ($r/D = 4.0$) begins travelling outward while rotating clockwise and getting stronger (state (a)). After this a new fluid having a high-shear-rate descended from upstream comes into the gap between this vortex and the wall and merges onto the outside of the vortex. The additional

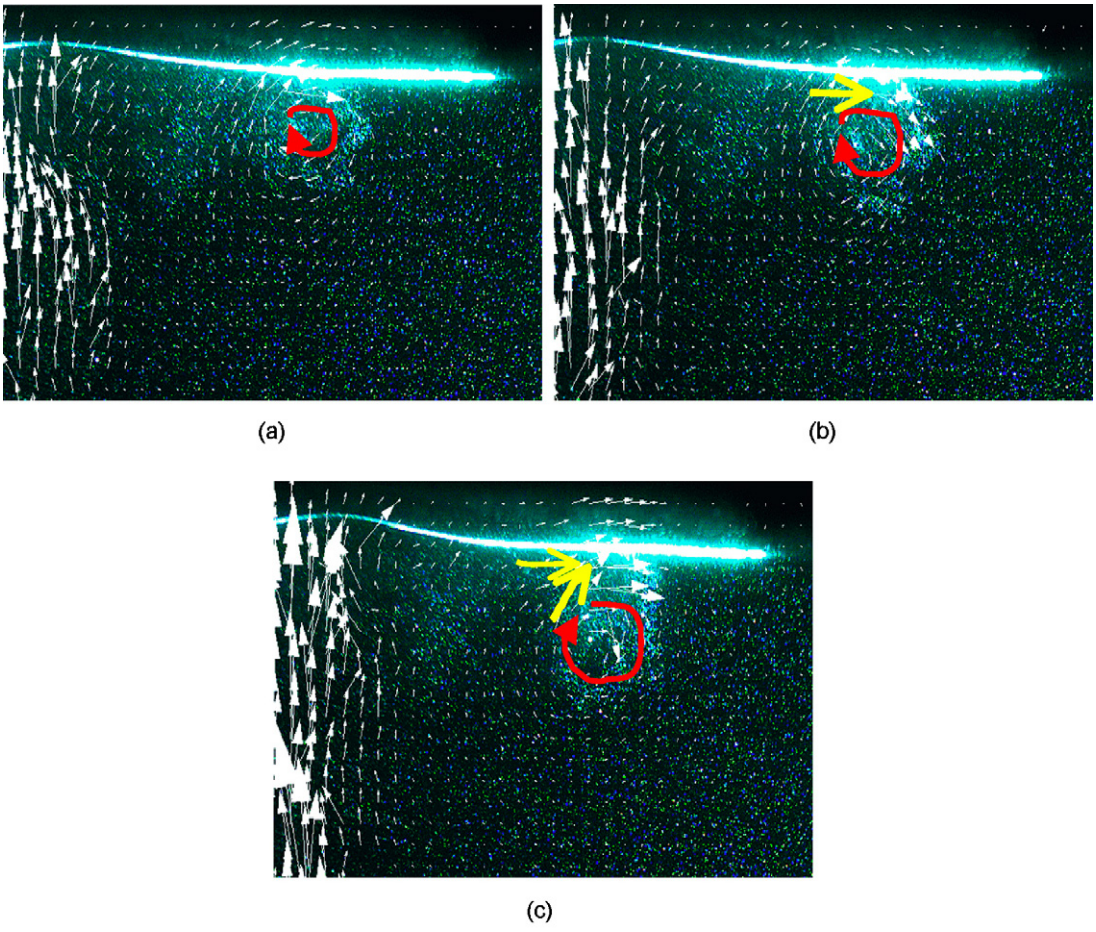

Fig. 22. Interactions between the flow and the elastic plate's motions: (a) $t = 880/1500$ s after valve open, (b) $t = 910/1500$ s after valve open and (c) $t = 968/1500$ s after valve open.

fluid plays like a whip on the vortex producing an additional rotational force and some part of the additional fluid that has high-shear-rate rides on the vortex and begins rotating together (state (b)). The additional high-shear-rate fluid meets a new high-shear-rate fluid coming from upstream after rotating around the original vortex. Eventually, newly merged fluid and the previous high-shear-rate fluid generate a strong normal force to the elastic plate. This is the reason why the elastic plate goes upward slightly (state (c)). Ellen and Tu reported the shear stress plays an important role in jets stripping process [5]. The results in this study show consistency with their results.

4. Conclusions

A simultaneous measurement system that could measure three-dimensional flow motions near the elastic plate and the 6-degree-of-freedom motions of a flexible plate has been constructed successfully for experiments on a pulsed impinging jet having an elastic wall.

In macroscopic experiments with $z/D = 2.3$, the flow fields and the motion fields obtained by 3D-PTV and 6DOF-motion tracking system showed qualitatively reasonable results. There was a reverse flow under the stagnation flow when the elastic plate went downward, and the structure of the reverse flow was well reconstructed by the results obtained by 3D-PTV. It has shown that the reverse flow near the stagnation region is due to the fact that rebounding of the elastic plate pushed the flow downward. This can be regarded as one of the most conspicuous FSI phenomenon.

In microscopic experiments with $z/D = 6.0$, the flow fields and the motion fields were obtained by 2D-PIV on the centre section of the jet and by 6DOF-motion tracking system with higher time and spatial resolution in order to investigate FSI near the elastic wall quantitatively. In case of $z/D = 6.0$, the elastic motion had longer periods of high frequency than in the case of $z/D = 2.3$. This implies that the vortices descended from the jet nozzle become more unstable near the stagnation region than in $z/D = 2.3$, and which eventually makes the elastic plate fluctuate with high frequency. The motion profile of the elastic plate was a 'bell shape' within the region of $r/D < 4.0$. This implies that the displacements of the plate are relatively smaller than in the region of $r/D < 4.0$. It was microscopically and schematically shown that the vortex merging phenomena produced a normal force onto the elastic wall, which makes the wall fluctuate locally.

For both cases of $z/D = 2.3$ and 6.0, a slight negative displacement was seen at the beginning of jet blowing. It is construed that there is a 'slight pressure drop' near the stagnation point due to the fact that the fluid from the jet nozzle produced an entrainment of the surrounding fluids, which makes an increase of mass flow rate and this increased mass sweeps outward along the elastic wall, eventually producing a 'pressure drop' near the stagnation point.

As additional results from the pulsed jet experiments with the elastic wall, it seems that the vortex separations over the wall occur earlier than in the case of a rigid wall. Further, the traveling speed and the size of the vortex were slower and larger, respectively, than in the case of the rigid wall. Interesting phenomenon is that the vortices came from the stagnation point have a tendency of moving farer away from the wall in the case of the rigid wall while they are passing near the wall toward downstream.

Acknowledgment

The paper was supported by Korea Research Foundation Grant (KRF-2004-002-D00082).

References

[1] H. Choi, Splitting method for the combined formulation of the fluid-particle problem, Comp. Methods Appl. Mech. Eng. 190 (11/12) (2000) 1367–1378.
[2] H.H. Hu, D.D. Josheph, Direct simulation of fluid particle motions, Theor. Comput. Fluid Dyn. 3 (1992) 285–306.
[3] H.H. Hu, Direct simulation of flows of solid–liquid mixtures, Int. J. Multiphase Flow 22 (1996) 335–352.
[4] H.G. Choi, D. Joheph, Fluidization by lift of 300 circular particles in plane Poiseuille flow by direct numerical simulation, J. Fluid Mech. 438 (2001) 101–128.
[5] C.H. Ellen, C.V. Tu, An analysis of jet stripping of liquid coatings, ASME J. Fluids Eng. 106 (1984) 399–404.
[6] D.J. Phares, G.T. Smedley, R.C. Flagan, The wall shear stress produced by the normal impingement of a jet on a flat surface, J. Fluid Mech. 418 (2000) 351–375.
[7] T. Cziesla, G. Biswas, H. Chattopadhyay, N.K. Mitra, Large-eddy simulation of flow and heat transfer in an impinging slot jet, Int. J. Heat Fluid Flow 22 (2001) 500–508.
[8] D.H. Doh, D.H. Kim, K.R. Cho, Y.B. Cho, T. Saga, T. Kobayashi, Development of GA based 3D-PTV technique, J. Visualization 5 (3) (2002) 243–254.
[9] D.H. Doh, T.G. Hwang, H.J. Jo, A study on developments of three-dimensional measurement system for flow–structure interactions using digital image processing, Korean J. Ocean Eng. Technol. 18 (4) (2004) 1–7.
[10] R.J. Adrian, R.J. Adrian, Particle-imaging techniques for experimental fluid mechanics, Annu. Rev. Fluid Mech. 23 (1991) 261–304.